coatings

MDPI

Article

Corrosion Behavior of N80 Steel Under Coalbed Methane Conditions

Jian Liu [1], Shijun Chen [1,*], Manxiang Li [1], Baojun Zheng [2], Chaoming Wang [2], Juantao Zhang [2], Ning Liu [3] and Xiaofei Cao [4,*]

[1] School of Chemistry and Chemical Engineering, Xi'an Petroleum University, Xi'an 710065, China; liujian_7777777@163.com (J.L.); limanxiang666@163.com (M.L.)
[2] State Key Laboratory of Oil and Gas Equipment, Xi'an 710077, China; 13619160082@163.com (B.Z.); wangcm06@cnpc.com.cn (C.W.); zhangjuantao@cnpc.com.cn (J.Z.)
[3] Oil & Gas Technology Research Institute, PetroChina Changqing Oilfield Branch, Xi'an 710018, China; liuning_cq@petrochina.com.cn
[4] School of Mechanical Engineering, Xi'an Petroleum University, Xi'an 710065, China
* Correspondence: csjun@xsyu.edu.cn (S.C.); caoxiaofei@xsyu.edu.cn (X.C.)

Highlights

What are the main findings?

- Increasing the nominal CO_2 partial pressure increased uniform corrosion but markedly reduced the maximum pitting corrosion rate of N80 steel.
- Increasing the nominal O_2 partial pressure accelerated both uniform corrosion and maximum local penetration and promoted cracking and spallation of the surface corrosion products.
- Increasing the Cl^- concentration suppressed average uniform corrosion but shifted the dominant damage mode toward severe localized pitting.
- The uniform corrosion rate peaked at 60 °C, whereas the maximum pitting corrosion rate increased continuously with temperature.
- The severity of localized corrosion was closely related to the surface coverage and visible integrity of $FeCO_3$-containing corrosion-product regions.

What are the implications of the main findings?

- Integrity assessments under CO_2-containing conditions should consider both average wall thinning and maximum local penetration.
- Oxygen ingress should be strictly controlled to limit the simultaneous development of uniform and localized corrosion.
- High-salinity formation water requires targeted pitting protection and inspection methods capable of detecting localized wall loss.
- Intermediate- and high-temperature well sections require differentiated monitoring of uniform wall thinning and pit propagation.
- Integrating SEM morphology with XRD phase identification provides a more reliable basis for evaluating the protective contribution of corrosion-product layers.

Abstract

The corrosion behavior of N80 steel in a simulated coalbed–methane environment was investigated in a high-temperature, high-pressure autoclave. Uniform corrosion and maximum pit depth were quantified by weight-loss measurements and ultra-depth-of-field three-dimensional microscopy, respectively, while SEM, EDS, and XRD were used to characterize the morphology, elemental composition, and crystalline phases of the surface corrosion products. A one-factor-at-a-time design was applied at a constant total pressure

Check for updates

Received: 19 July 2026
Revised: 12 August 2026
Accepted: 18 August 2026
Published: 20 August 2026

Copyright: © 2026 by the authors. Licensee MDPI, Basel, Switzerland. This article is an open access article distributed under the terms and conditions of the Creative Commons Attribution (CC BY) license.

of 10 MPa to evaluate the effects of nominal CO_2 partial pressure (0.10–1.00 MPa), nominal O_2 partial pressure (0–0.40 MPa), Cl^- concentration (3–187 g/L), and temperature (40–75 °C). Increasing the nominal CO_2 partial pressure raised the uniform corrosion rate from 0.712 to 0.930 mm/a but reduced the maximum pitting corrosion rate from 1.691 to 0.280 mm/a, while $FeCO_3$-containing surface coverage increased. Increasing the nominal O_2 partial pressure intensified both corrosion modes; at 0.40 MPa, the uniform and maximum pitting corrosion rates reached 1.446 and 2.202 mm/a, respectively, and the corrosion-product layer exhibited extensive cracking and spallation. Increasing the Cl^- concentration reduced the uniform corrosion rate from 1.078 to 0.839 mm/a but increased the maximum pitting corrosion rate from 0.474 to 1.807 mm/a, indicating a shift in the principal damage risk from average metal loss to localized penetration. The uniform corrosion rate reached a maximum of 1.516 mm/a at 60 °C, whereas the maximum pitting corrosion rate increased continuously to 2.202 mm/a at 75 °C. XRD identified Fe, $FeCO_3$, Fe_2O_3, Fe_3O_4, and FeOOH. The persistent Fe substrate reflections, interpreted together with the SEM observations, revealed spatially heterogeneous corrosion-product coverage. These results show that the protective contribution of $FeCO_3$-containing products depends on their surface coverage and visible integrity rather than on phase presence alone. The findings support stringent oxygen-ingress control, targeted pitting protection in high-salinity environments, and enhanced corrosion surveillance of intermediate- and high-temperature well sections.

Keywords: N80 steel; coalbed methane; uniform corrosion; pitting corrosion; corrosion-product layer; corrosion mechanism

1. Introduction

China has abundant coalbed–methane resources and is among the world's major holders of such resources [1]. Their efficient development can improve natural gas utilization, reduce methane-related environmental impacts, and mitigate geological hazards associated with coal seams. Owing to its favorable cost and mechanical properties, carbon steel is widely used for tubing, casing, and pipelines in oil and gas production. However, it is susceptible to corrosion in CO_2-containing aqueous environments [2]. During coalbed–methane production, casing and tubing strings may be exposed for extended periods to high-pressure gas, saline produced water, oxygen introduced during operational interventions, and temperature gradients. The resulting uniform wall thinning and localized penetration threaten wellbore integrity and safe operation [3,4].

Corrosion of tubing and casing has been investigated from the perspectives of environmental chemistry, electrochemical reactions, corrosion-product formation, and material response. CO_2 is a major corrosive species in many wellbore environments. Hou et al. [5] used a high-temperature, high-pressure autoclave to simulate a deep shale-gas well and found that increasing CO_2 pressure increased the corrosion rate of P110 tubing. Other studies have likewise shown that CO_2 accelerates carbon-steel corrosion in the presence of water [6,7]. Oxygen is another important factor. In CO_2/O_2-containing systems, oxygen reduction can increase the cathodic reaction rate and intensify both uniform and localized attack [8–10]. Wang et al. [11] reported that increasing O_2 promoted corrosion of X80 steel and damaged the corrosion-product layer, whereas Song [12] showed that corrosion behavior depends on the relative availability of CO_2 and O_2. Cl^- and dissolved O_2 in formation water may also act synergistically. Leng et al. [13] found that 0–3000 mg/L Cl^- promoted localized corrosion of L245N steel in a CO_2-O_2-Cl^- environment, whereas

3000–5000 mg/L Cl^- inhibited the cathodic process. Sun et al. [14] demonstrated that pH and dissolved oxygen affected the electrochemical behavior and oxide-film characteristics of 304 stainless steel in high-temperature water. Temperature also influences reaction kinetics, gas solubility, mass transfer, and the dissolution and precipitation of corrosion products [15,16]. Dong et al. [17] identified temperature as an important factor governing corrosion of N80 tubing. Although the individual effects of CO_2, O_2, Cl^-, and temperature have been widely reported, few studies have compared uniform corrosion, maximum local penetration, and corrosion-product-layer evolution of N80 steel within a single, internally consistent high-pressure framework representative of coalbed–methane service and field-produced-water chemistry.

To address this gap, this study systematically evaluated the individual effects of nominal CO_2 partial pressure, nominal O_2 partial pressure, Cl^- concentration, and temperature on N80 steel at a constant total pressure of 10 MPa in simulated produced water representative of the target field. Weight-loss and maximum-pit-depth measurements were combined with SEM, EDS, and XRD to compare average wall loss and maximum local penetration within the same experimental framework and to relate their contrasting responses to changes in corrosion-product morphology and phase composition. The resulting correlations among environmental conditions, $FeCO_3$-containing surface coverage, visible cracking and spallation, and localized-corrosion severity provide an experimental basis for corrosion-risk assessment and integrity management of N80 tubing in coalbed–methane wells.

2. Experimental

2.1. Experimental Materials, Apparatus, and Media

N80 tubing steel was used as the test material, and its chemical composition is listed in Table 1. Rectangular specimens measuring 50 mm × 10 mm × 3 mm were prepared. Corrosion tests were conducted in a high-temperature, high-pressure Hastelloy C276 autoclave (TFCZ5-25/450, Wuxi Angong Kemao Equipment Technology Co., Ltd., Wuxi, China). The test medium was simulated formation water prepared based on the major ionic species detected in produced water from the target coalbed–methane well; its initial ionic composition is given in Table 2.

Table 1. Chemical composition of N80 steel (wt.%).

C	Si	Mn	P	S	Cr	Mo	Ni	V	Cu	Al	Fe
0.31	0.26	1.32	0.0052	0.0067	0.060	0.014	0.011	0.0043	0.014	0.017	Bal.

Note: Fe represents the balance of the alloy composition.

Table 2. Initial ionic composition of the simulated formation water (mg/L).

K^+	Na^+	Ca^{2+}	Mg^{2+}	Ba^{2+}	Sr^{2+}
34.5	61,894.0	371.0	76.0	15.5	279.0
NH_4^+	Fe^{3+}	Cl^-	SO_4^{2-}	HCO_3^-	CO_3^{2-}
56.0	88.0	93,819.9	236.71	4603.6	5.0

Note: $FeCl_3$ was used as the Fe^{3+} source in the initial solution formulation. The listed Fe^{3+} concentration was calculated from the amount added during solution preparation and represents the initial composition before the 72 h exposure.

2.2. Experimental Methods

A one-factor-at-a-time design was adopted: one environmental variable was varied while the remaining variables were maintained at their baseline values. Before exposure, the N80 specimens were sequentially ground with 400-, 800-, and 1200-grit silicon carbide papers, ultrasonically cleaned with acetone and anhydrous ethanol, dried, and weighed on an electronic balance (BP221S, Sartorius AG, Göttingen, Germany) with a resolution of 0.1 mg. The specimen dimensions were measured with a vernier caliper to determine the exposed area. Simulated formation water was prepared with deionized water according to Table 2. For the Cl^--concentration series, only the amount of NaCl was varied; all other salt additions were kept constant. Consequently, the Na^+ concentration and ionic strength increased with the Cl^- concentration. $FeCl_3$ was added at 256.67 mg/L, corresponding to 88 mg/L Fe^{3+} in the initial formulation. The specimens and test solution were placed in the autoclave, which was sealed and thoroughly purged with N_2 to remove oxygen from the system. For the 0 MPa O_2 condition, no O_2 was added after purging. After the autoclave reached the target temperature, CO_2 and O_2 were sequentially introduced to establish the nominal partial pressures listed in Table 3. N_2 was subsequently added as the balance gas until the total pressure reached 10 MPa. The nominal N_2 partial pressure was calculated as $P_{N2,nom} = 10 - P_{CO2,nom} - P_{O2,nom.}$ Each test lasted 72 h. Four specimens were exposed under each condition: three were used for weight-loss and pit-depth measurements, and one was reserved for SEM/EDS and XRD characterization. After exposure, the autoclave was cooled and depressurized slowly. The characterization specimen was gently rinsed with anhydrous ethanol, dried, and stored in a desiccator; no water rinsing, brushing, or chemical cleaning was applied. The remaining specimens were descaled in a solution containing 500 mL hydrochloric acid, 3.5 g hexamethylenetetramine, and 500 mL deionized water, reweighed, and used to calculate the uniform corrosion rate. After descaling, the 50 mm × 10 mm principal surface showing the most severe visible corrosion on each of the three specimens was scanned with an ultra-depth-of-field three-dimensional microscope (Smartzoom 5, Carl Zeiss Microscopy GmbH, Jena, Germany). The evaluated area was 500 mm^2 per specimen and 1500 mm^2 per condition. The deepest pit on each specimen was identified from the three-dimensional profile, and d_{max} in Equation (2) was defined as the greatest depth measured among the three specimens. The three-dimensional profilometry measurements were designed specifically for maximum pit depth assessment. A validated full-field pit-segmentation and counting procedure was not applied during data acquisition; therefore, the present dataset is used to quantify d_{max} and the corresponding maximum pitting corrosion rate rather than pit density or statistical pit size distributions.

$$v_c = \frac{87600 \times (W_0 - W_1)}{S \times t \times \rho} \quad (1)$$

where v_c is the uniform corrosion rate (mm/a); 87,600 is the unit-conversion factor; W_0 and W_1 are the specimen masses before and after exposure (g), respectively; ρ is the density (g/cm^3); S is the exposed area (cm^2); and t is the exposure time (h).

$$v_p = \frac{d_{max} \times 8760}{t} \quad (2)$$

where v_p is the maximum pitting corrosion rate (mm/a); 8760 is the unit-conversion factor (24 h/day × 365 days/a); d_{max} is the maximum pit depth (mm); and t is the exposure time (h). The values calculated using Equation (2) are annualized by linearly extrapolating the maximum pit depths measured after 72 h. They are used solely as comparative indicators of localized-corrosion severity and should not be interpreted as predictions of pit penetration

after one year of service. Because pit initiation and propagation are time-dependent and generally nonlinear, linear extrapolation may overestimate long-term pitting rates.

Table 3. Test matrix and nominal partial pressures at a constant total pressure of 10 MPa.

Autoclave Run	Nominal CO_2 Partial Pressures/MPa	Nominal O_2 Partial Pressures/MPa	Nominal N_2 Balance Pressure/MPa	Cl^- Concentration/(g/L)	Temperature/°C	Total Pressure /MPa
1	0.10	0.20	9.70	95	75	10
2	0.55	0.20	9.25	95	75	10
3	1.00	0.20	8.80	95	75	10
4	0.55	0.00	9.45	95	75	10
5	0.55	0.40	9.05	95	75	10
6	0.55	0.20	9.25	3	75	10
7	0.55	0.20	9.25	187	75	10
8	0.55	0.40	9.05	95	40	10
9	0.55	0.40	9.05	95	60	10

Note: The CO_2 and O_2 values are reported as nominal partial pressures. N_2 was used as the balance gas to maintain a total pressure of 10 MPa, with $P_{N2,nom} = 10 - P_{CO2,nom} - P_{O2,nom}$. For the Cl^- series, only the NaCl addition was varied; therefore, the Na^+ concentration and ionic strength changed simultaneously. Autoclave Run 2 (0.55 MPa CO_2, 0.20 MPa O_2, 95 g/L Cl^-, 75 °C) served as the common reference condition for the CO_2, O_2, and Cl^- series, whereas Autoclave Run 5 (0.55 MPa CO_2, 0.40 MPa O_2, 95 g/L Cl^-, 75 °C) was shared by the O_2 and temperature series. Repeated EDS and XRD datasets therefore originate from the same autoclave exposures.

For each condition, the uniform corrosion rate is reported as the mean ± standard deviation of three replicate specimens exposed within the same autoclave run (SD, $n = 3$). The error bars, where present in Figures 1–8, represent the SD. The maximum pitting corrosion rate was calculated from the deepest pit among the same three specimens and is reported as a single conservative maximum value. Because this parameter is a maximum rather than a replicate mean, no standard deviation or confidence interval was assigned. Both corrosion-rate metrics therefore represent 72 h time-averaged or annualized comparative values rather than time-resolved corrosion kinetics.

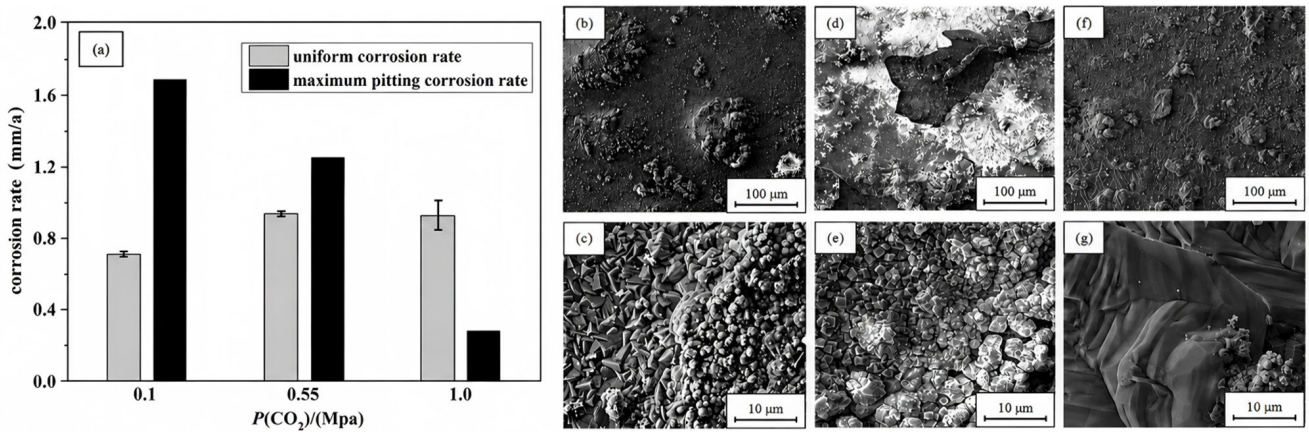


Figure 1. Corrosion rates and surface morphologies of N80 steel at different CO_2 partial pressures: (**a**) uniform and maximum pitting corrosion rates; (**b**,**c**) 0.10 MPa; (**d**,**e**) 0.55 MPa; (**f**,**g**) 1.00 MPa; (**b**,**d**,**f**) 100×; and (**c**,**e**,**g**) 1000×. Error bars denote the SD of the uniform corrosion rates ($n = 3$); maximum pitting corrosion rates are reported as single maximum values. Panels (**b**,**d**,**f**) show the 100 × EDS acquisition fields corresponding to Table 4.

Table 4. EDS atomic percentages of corrosion-product regions on N80 steel at different CO_2 partial pressures.

CO_2 Partial Pressure/MPa	Atomic Percentage/%					
	C	O	Na	Cl	Ca	Fe
0.1	7.99	54.09	/	1.40	/	36.52
0.55	7.02	65.68	/	2.07	/	25.23
1	18.61	51.82	2.95	1.33	3.07	22.22

Note: The EDS values are local, semi-quantitative atomic percentages obtained from selected analysis regions and are reported as generated by the instrument software. The number of decimal places does not imply an analytical accuracy of 0.01 at.%. "/" indicates that the element was not detected in the analyzed region. The data at 0.55 MPa CO_2 correspond to Autoclave 2 and are identical to the shared reference-condition data reported at 0.20 MPa O_2 in Table 5 and at 95 g/L Cl^- in Table 6.

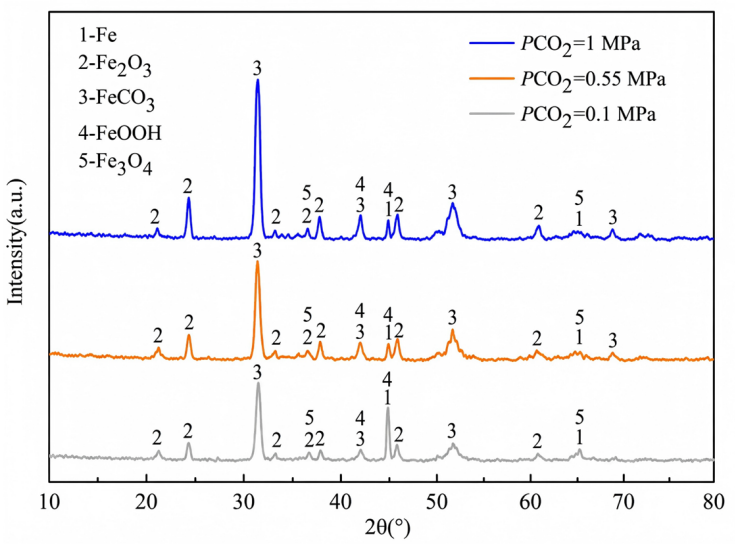


Figure 2. XRD patterns of corrosion products on N80 steel at different CO_2 partial pressures.

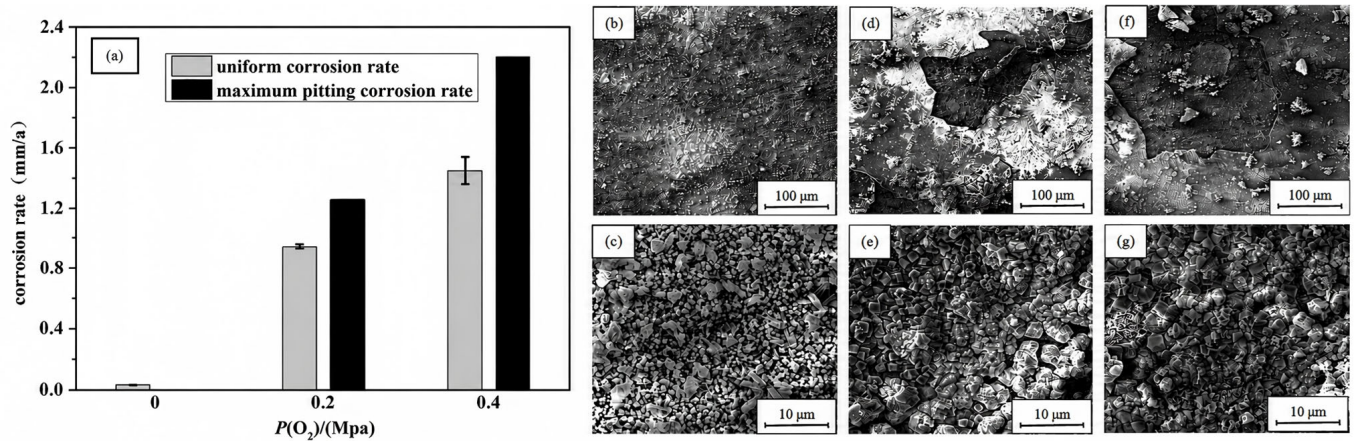


Figure 3. Corrosion rates and surface morphologies of N80 steel at different O_2 partial pressures: (**a**) uniform and maximum pitting corrosion rates; (**b**,**c**) 0 MPa; (**d**,**e**) 0.20 MPa; (**f**,**g**) 0.40 MPa; (**b**,**d**,**f**) 100×; and (**c**,**e**,**g**) 1000×. Error bars denote the SD of the uniform corrosion rates (n = 3); maximum pitting corrosion rates are reported as single maximum values. Panels (**b**,**d**,**f**) show the 100 × EDS acquisition fields corresponding to Table 5.

Table 5. EDS atomic percentages of corrosion-product regions on N80 steel at different O_2 partial pressures.

O_2 Partial Pressure/MPa	Atomic Percentage/%					
	C	O	Na	Cl	Ca	Fe
0	14.87	53.31	11.34	7.52	9.37	3.59
0.2	7.02	65.68	/	2.07	/	25.23
0.4	16.39	64.09	0.79	/	2.03	16.70

Note: The EDS values are local, semi-quantitative atomic percentages obtained from selected analysis regions and are reported as generated by the instrument software. The number of decimal places does not imply an analytical accuracy of 0.01 at.%. "/" indicates that the element was not detected in the analyzed region. The data at 0.20 MPa O_2 correspond to Autoclave 2 and are also reported in Tables 4 and 6. The data at 0.40 MPa O_2 correspond to Autoclave 5 and are also reported at 75 °C in Table 7.

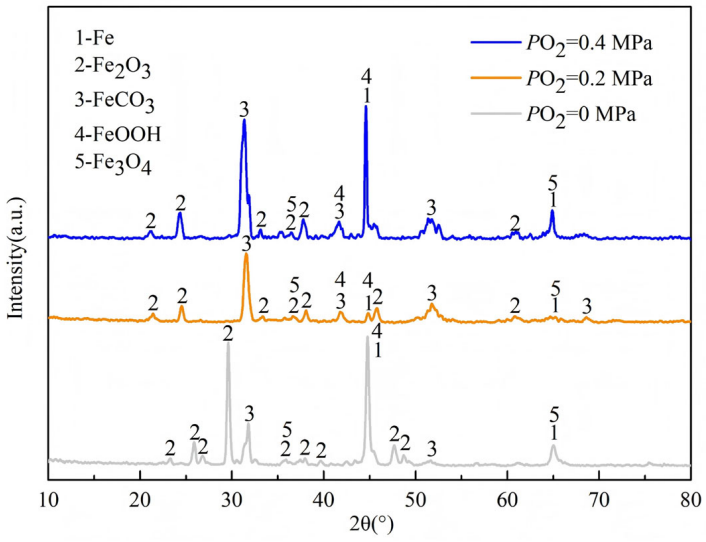


Figure 4. XRD patterns of corrosion products on N80 steel at different O_2 partial pressures.

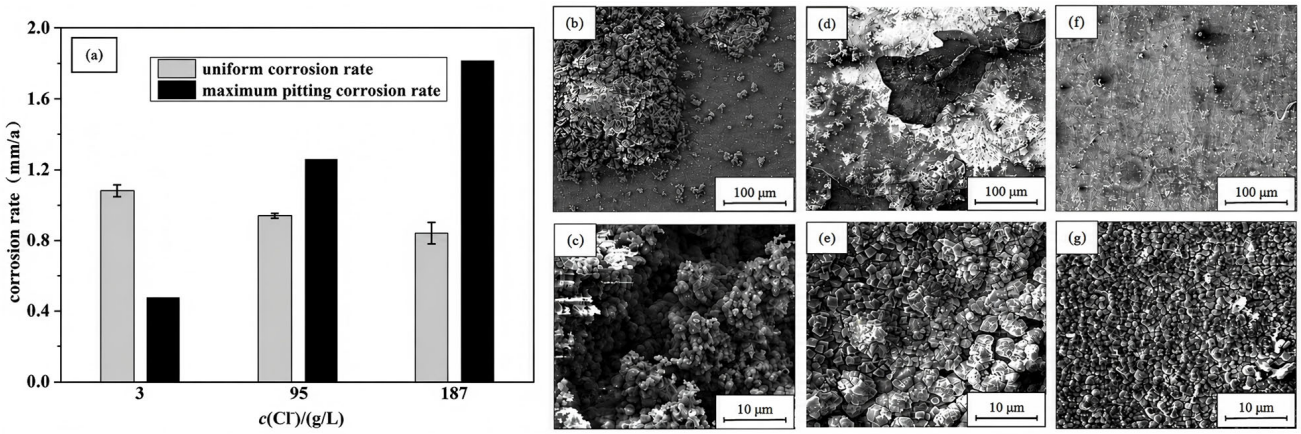


Figure 5. Corrosion rates and surface morphologies of N80 steel at different Cl^- concentrations: (**a**) uniform and maximum pitting corrosion rates; (**b**,**c**) 3 g/L; (**d**,**e**) 95 g/L; (**f**,**g**) 187 g/L; (**b**,**d**,**f**) 100×; and (**c**,**e**,**g**) 1000×. Error bars denote the SD of the uniform corrosion rates (n = 3); maximum pitting corrosion rates are reported as single maximum values. Panels (**b**,**d**,**f**) show the 100 × EDS acquisition fields corresponding to Table 6.

Table 6. EDS atomic percentages of corrosion-product regions on N80 steel at different Cl^- concentrations.

Cl^- Concentration/(g/L)	Atomic Percentage/%					
	C	O	Na	Cl	Ca	Fe
3	12.00	55.45	/	/	0.80	31.75
95	7.02	65.68	/	2.07	/	25.23
187	15.17	62.86	0.97	1.03	6.36	13.61

Note: The EDS values are local, semi-quantitative atomic percentages obtained from selected analysis regions and are reported as generated by the instrument software. The number of decimal places does not imply an analytical accuracy of 0.01 at.%. "/" indicates that the element was not detected in the analyzed region. The data at 95 g/L Cl^- correspond to Autoclave 2 and are identical to the shared reference-condition data reported in Tables 4 and 5.

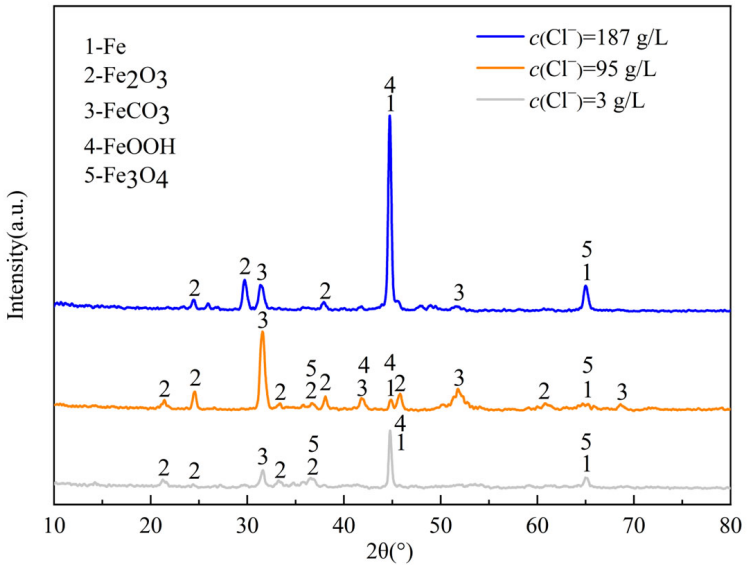


Figure 6. XRD patterns of corrosion products on N80 steel at different Cl^- concentrations.

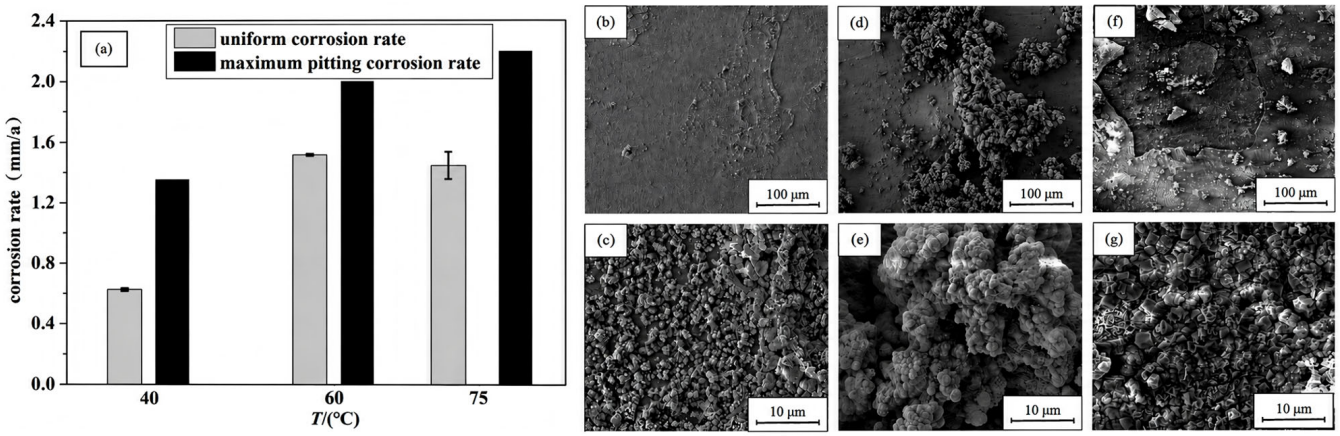


Figure 7. Corrosion rates and surface morphologies of N80 steel at different temperatures: (**a**) uniform and maximum pitting corrosion rates; (**b**,**c**) 40 °C; (**d**,**e**) 60 °C; (**f**,**g**) 75 °C; (**b**,**d**,**f**) 100×; and (**c**,**e**,**g**) 1000×. Error bars denote the SD of the uniform corrosion rates (n = 3); maximum pitting corrosion rates are reported as single maximum values. Panels (**b**,**d**,**f**) show the 100 × EDS acquisition fields corresponding to Table 7.

Table 7. EDS atomic percentages of corrosion-product regions on N80 steel at different temperatures.

Temperature/°C	Atomic Percentage/%					
	C	O	Na	Cl	Ca	Fe
40	5.27	51.57	/	0.24	4.25	38.67
60	5.98	48.24	4.24	4.72	0.54	36.28
75	16.39	64.09	0.79	/	2.03	16.70

Note: The EDS values are local, semi-quantitative atomic percentages obtained from selected analysis regions and are reported as generated by the instrument software. The number of decimal places does not imply an analytical accuracy of 0.01 at.%. "/" indicates that the element was not detected in the analyzed region. The data at 75 °C correspond to Autoclave 5 and are identical to those reported at 0.40 MPa O_2 in Table 5.

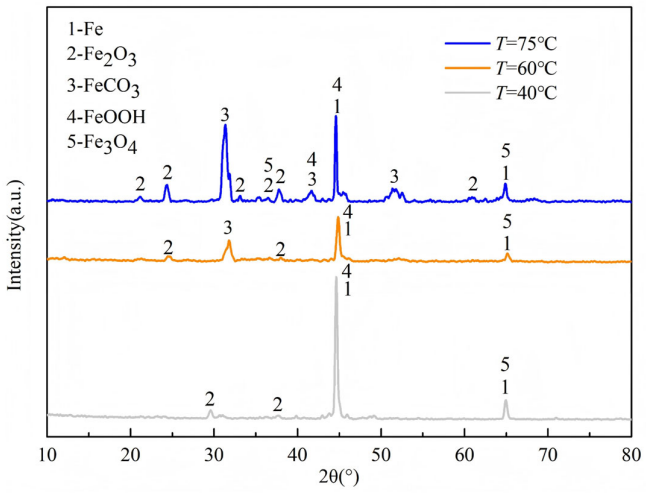


Figure 8. XRD patterns of corrosion products on N80 steel at different temperatures.

Surface morphology and elemental composition were characterized by SEM coupled with EDS (Sigma 360, Carl Zeiss Microscopy GmbH, Jena, Germany). For each condition, the EDS area analysis covered the entire field of view of the corresponding 100 × SEM image; the values in Tables 4–7 are therefore local, semi-quantitative averages for the displayed fields. Crystalline phases were examined ex situ using an X-ray diffractometer (XRD-6000, Shimadzu Corporation, Kyoto, Japan) in a conventional θ-2θ configuration over a 2θ range of 10–80°. The patterns in Figures 2, 4, 6 and 8 were indexed as follows: 1, Fe substrate; 2, Fe_2O_3; 3, $FeCO_3$; 4, FeOOH; and 5, Fe_3O_4. Because conventional θ-2θ XRD detects diffraction from both the surface corrosion products and the underlying steel, the substrate-peak intensity was interpreted together with the surface coverage observed by SEM.

The test levels in Table 3 were selected from operating records and produced-water characteristics of the target coalbed–methane block. Nominal CO_2 partial pressures of 0.10, 0.55, and 1.00 MPa represent the lower, intermediate, and upper portions of the block-specific range. Nominal O_2 partial pressures of 0, 0.20, and 0.40 MPa represent the deoxygenated reference condition and the intermediate and upper oxygen-bearing conditions. Cl^- concentrations of 3, 95, and 187 g/L represent low-, field-representative-, and high-salinity conditions, respectively, with 95 g/L used as the common baseline. Temperatures of 40, 60, and 75 °C represent the lower, intermediate, and upper portions of the service-temperature range. N_2 was used as the balance gas to maintain a total pressure of 10 MPa in every test.

At a total pressure of 10 MPa, the CO_2–O_2–N_2 mixture may deviate from ideal-gas behavior. The equilibrium dissolution of component i is therefore more rigorously governed by its fugacity, $f_i = \varphi_i y_i P$, where φ_i is the fugacity coefficient, y_i is the gas-phase mole

fraction, and P is the total pressure. N_2 served as the balance gas and did not participate directly in the corrosion reactions; nevertheless, at 10 MPa, the large N_2 fraction may influence the component fugacity coefficients and gas–liquid equilibrium.

3. Results and Discussion

Unless otherwise stated, the CO_2 and O_2 values discussed below refer to the nominal partial pressures listed in Table 3.

The initially added Fe^{3+} may have participated in early cathodic reduction and subsequently transformed into Fe^{2+} or Fe-containing precipitates. Because the same $FeCl_3$ concentration was used in every test, its influence constituted a common background condition in comparisons of CO_2 partial pressure, O_2 partial pressure, Cl^- concentration, and temperature. The following mechanistic discussion integrates the measured corrosion rates, maximum pit depths, SEM morphologies, EDS elemental signals, and XRD phases with established corrosion theory.

3.1. Effect of Nominal CO_2 Partial Pressure on Corrosion Behavior

Autoclave Runs 1, 2, and 3 were compared at CO_2 partial pressures of 0.10, 0.55, and 1.00 MPa, respectively; the other conditions were 0.20 MPa O_2, 95 g/L Cl^-, 75 °C, and a total pressure of 10 MPa. As the CO_2 partial pressure increased from 0.10 to 1.00 MPa, the uniform corrosion rate increased from 0.712 to 0.930 mm/a, whereas the maximum pitting corrosion rate decreased from 1.691 to 0.280 mm/a. A quantitative comparison with previous tubing steel studies further places these values in context. Cheng et al. reported a uniform corrosion rate of 0.081 mm/a for N80 steel at 80 °C, 0.10 MPa CO_2, and 168 h in simulated formation water [18]. At the same nominal CO_2 partial pressure of 0.10 MPa, the present study yielded 0.712 mm/a at 75 °C and 72 h, approximately 8.8 times the value reported by Cheng et al. The substantially higher rate is associated with the different environmental conditions, particularly the presence of a nominal O_2 partial pressure of 0.20 MPa and the much higher Cl^- concentration of 95 g/L in the present system, together with differences in water chemistry and exposure duration. Hou et al. reported a corrosion rate of approximately 0.6650 mm/a for P110 tubing under a CO_2-containing wellhead condition at 50 °C, 10 MPa total pressure, 1% CO_2, 10 g/L Cl^-, and 168 h [5], which is of the same order of magnitude as the 0.712 mm/a measured here. These comparisons confirm that the absolute corrosion rate is highly sensitive to the combined gas composition and aqueous chemistry, while the trend of increasing uniform corrosion with greater CO_2 availability remains consistent with previous observations.

The corrosion-product morphology changed markedly with CO_2 partial pressure (Figure 1). At 0.10 MPa, loose products covered only part of the surface, leaving extensive areas of substrate exposed. At 0.55 MPa, cracking and spallation produced large exposed regions. At 1.00 MPa, the examined surface exhibited broader product coverage and fewer large exposed areas. EDS detected mainly Fe, C, and O, and the local C fraction was highest at 1.00 MPa (Table 4). XRD identified Fe, $FeCO_3$, Fe_2O_3, Fe_3O_4, and FeOOH (Figure 2), with $FeCO_3$ reflections becoming progressively more prominent as the CO_2 partial pressure increased. At 1.00 MPa, the Fe substrate reflections near 44.7° and 65° were attenuated but remained visible, showing that the diffraction pattern contained contributions from both the corrosion products and the underlying steel. Taken together, the SEM and XRD results indicate broader, but spatially heterogeneous, $FeCO_3$-containing coverage. The weak oxide and oxyhydroxide reflections may reflect the oxygen-bearing exposure, transformation of the initially added Fe(III)-containing species, and oxidation during post-test handling. The local Na, Cl, and Ca signals detected by EDS were attributed partly to salts retained from the highly saline solution during drying.

Increasing the CO_2 partial pressure intensifies two competing processes. First, greater CO_2 dissolution increases the abundance of carbonic-acid species, thereby accelerating cathodic reduction and iron dissolution; electrochemical studies have also shown that CO_2 and carbonate species affect the anodic dissolution of carbon steel [19]. This effect accounts for the continuous increase in the uniform corrosion rate. Second, the increased Fe^{2+} supply generated by corrosion, together with carbonate species in solution, favors $FeCO_3$ precipitation and the growth of $FeCO_3$-containing surface products [20]. Between 0.10 and 0.55 MPa, the corrosive effect of the solution remained dominant because the product layer was cracked and discontinuous, resulting in a rapid increase in uniform corrosion. At 1.00 MPa, the greater $FeCO_3$ contribution and broader surface coverage increased resistance to local mass transfer; consequently, the uniform corrosion rate continued to increase, but by a smaller increment. The maximum pitting corrosion rate exhibited the opposite trend. At 0.10 MPa, extensive substrate exposure produced pronounced surface heterogeneity and favored localized dissolution. As the CO_2 partial pressure increased, broader $FeCO_3$-containing coverage reduced the number and persistence of exposed anodic sites and restricted access of the chloride-containing solution to the steel surface. Previous investigations of CO_2 corrosion have similarly linked the development and condition of $FeCO_3$ layers to the initiation and propagation of localized attack [21]. The progressive increase in surface coverage therefore explains the monotonic decrease in the maximum pitting corrosion rate.

3.2. Effect of Nominal O_2 Partial Pressure on Corrosion Behavior

Autoclave Runs 4, 2, and 5 were compared at O_2 partial pressures of 0, 0.20, and 0.40 MPa, respectively; the other conditions were 0.55 MPa CO_2, 95 g/L Cl^-, 75 °C, and a total pressure of 10 MPa. Both the uniform and maximum pitting corrosion rates increased monotonically with O_2 partial pressure, reaching 1.446 and 2.202 mm/a, respectively, at 0.40 MPa. Shi et al. likewise observed a pronounced increase in the corrosion rate of N80 steel after oxygen was introduced into a high-pressure CO_2- containing wellbore environment [22]. Under their test conditions of 70 °C, 10 MPa total pressure, 0.05 MPa CO_2, and 0.30 MPa O_2, the uniform corrosion rate reached 0.5232 mm/a. In comparison, the present study obtained 1.446 mm/a at 75 °C, 10 MPa total pressure, 0.55 MPa CO_2, and 0.40 MPa O_2, approximately 2.8 times the value reported by Shi et al. The difference in absolute magnitude reflects the higher CO_2 and O_2 availability and the different formation water chemistry in the present system. Nevertheless, both datasets quantitatively demonstrate the strong accelerating effect of oxygen on the corrosion of N80 steel under high-pressure CO_2-containing conditions. At 0 MPa O_2, fine corrosion-product grains covered much of the examined field, and the corrosion rate was low. At 0.20 MPa, extensive cracking and spallation exposed the substrate; at 0.40 MPa, the spalled regions expanded further. This progressive loss of surface-layer integrity coincided with simultaneous increases in average wall loss and maximum local penetration.

EDS and XRD further revealed changes in the corrosion products with O_2 partial pressure (Table 5 and Figure 4). At 0 MPa O_2, the analyzed field contained a low Fe fraction and relatively strong Na, Cl, and Ca signals, partly because of retained salts. XRD identified Fe, $FeCO_3$, Fe_2O_3, Fe_3O_4, and FeOOH. The weak oxygen-containing phases under the deoxygenated reference condition may reflect transformation of the initially added Fe(III)-containing species or oxidation during post-test handling. The local Fe atomic fraction increased from 3.59 at.% at 0 MPa to 25.23 at.% at 0.20 MPa and then decreased to 16.70 at.% at 0.40 MPa. Fe substrate reflections remained visible under all conditions, whereas the relative contributions of $FeCO_3$ and the oxygen-containing phases varied with O_2 partial pressure. No distinct crystalline NaCl phase was identified, consistent with the

localized EDS signals and the low overall abundance of retained salts within the larger XRD sampling area.

Under the 0 MPa O_2 condition, no O_2 was added after N_2 purging. The cathodic process was therefore governed primarily by reactions in the CO_2-containing aqueous phase, resulting in a low uniform corrosion rate and no measurable pit depth.

Increasing the O_2 partial pressure increases the oxygen available for cathodic reduction. The accelerated oxygen-reduction reaction raises the cathodic current and is balanced by faster anodic dissolution of iron, accounting for the increase in the uniform corrosion rate [23,24]. Oxygen also alters the composition and morphology of the surface products. Studies of CO_2-containing systems have shown that oxygen can destabilize $FeCO_3$-containing scales and promote localized attack [24–27]. In the present tests, the surface changed from fine-grained coverage at 0 MPa O_2 to coarse products, extensive cracking, and spallation at 0.20 and 0.40 MPa. The damaged regions exposed fresh steel and created differential surface conditions between covered and uncovered areas. Oxygen reduction on the surrounding surface can sustain anodic dissolution at these exposed sites, while Cl^- transport and local acidification promote pit propagation. Thus, accelerated cathodic kinetics and deterioration of the surface-product layer jointly explain the simultaneous increases in the uniform and maximum pitting corrosion rates.

3.3. Effect of Nominal Cl^- Concentration on Corrosion Behavior

Autoclave Runs 6, 2, and 7 were compared at Cl^- concentrations of 3, 95, and 187 g/L, respectively; the other conditions were 0.55 MPa CO_2, 0.20 MPa O_2, 75 °C, and a total pressure of 10 MPa. Only the NaCl addition was varied; consequently, the Na^+ concentration and ionic strength increased with the Cl^- concentration. As the Cl^- concentration increased from 3 to 187 g/L, the uniform corrosion rate decreased from 1.078 to 0.839 mm/a, whereas the maximum pitting corrosion rate increased from 0.474 to 1.807 mm/a. At 3 g/L, loose products were distributed locally. At 95 g/L, extensive cracking and spallation exposed the substrate. At 187 g/L, fine-grained corrosion products covered substantial portions of the examined surface, while isolated uncovered and damaged regions remained.

EDS detected mainly Fe, C, and O, and the local Fe fraction decreased as the Cl^- concentration increased (Table 6). XRD identified Fe, $FeCO_3$, Fe_2O_3, Fe_3O_4, and FeOOH (Figure 6). The $FeCO_3$ reflections were strongest at 95 g/L. At 187 g/L, these reflections weakened, whereas the Fe substrate reflections near 44.7° and 65° became dominant. Together with the SEM observations, the XRD pattern indicates a heterogeneous surface consisting of fine-grained corrosion-product regions and areas that contributed strongly to the substrate diffraction signal. This heterogeneous coverage is consistent with the coexistence of lower average uniform corrosion and severe maximum local penetration.

The opposite trends in uniform and localized corrosion arise from the combined effects of NaCl concentration, ionic strength, corrosion-product coverage, and pit chemistry. Increasing the NaCl concentration changes the solution activity coefficients and reduces the aqueous availability of CO_2 and O_2 through salting-out, thereby lowering the average cathodic reaction rate and contributing to the decrease in uniform corrosion at high salinity [28,29]. At the same time, Fe^{2+} released by anodic dissolution reacts with carbonate species to form $FeCO_3$-containing products, and the fine-grained product regions observed at 187 g/L can reduce metal loss in covered areas. Chloride nevertheless remains highly aggressive at localized sites. It accumulates at exposed or damaged regions, promotes the formation of soluble Fe-Cl species, and facilitates continued anodic dissolution [30–32]. Within an active pit, Fe^{2+} hydrolysis lowers the local pH, while Cl^- migration maintains electroneutrality, establishing an autocatalytic environment that sustains pit growth. Similar decoupling between reduced general corrosion and persistent localized attack has been

reported in high-chloride CO_2 systems [32–34]. Consequently, the high-salinity condition reduced average wall loss while allowing the deepest active pits to propagate rapidly.

3.4. Effect of Temperature on Corrosion Behavior

Autoclave Runs 8, 9, and 5 were compared at 40, 60, and 75 °C, respectively; the other conditions were 0.55 MPa CO_2, 0.40 MPa O_2, 95 g/L Cl^-, and a total pressure of 10 MPa. The uniform corrosion rate increased from 0.627 mm/a at 40 °C to 1.516 mm/a at 60 °C and then decreased slightly to 1.446 mm/a at 75 °C. In contrast, the maximum pitting corrosion rate increased continuously from 1.351 to 2.202 mm/a.

The surface morphology changed systematically with temperature (Figure 7). At 40 °C, loose products covered limited areas, leaving much of the substrate exposed. At 60 °C, coarse granular aggregates formed, with visible gaps and discontinuous coverage. At 75 °C, local spallation was more extensive, although some unspalled regions exhibited greater product coverage. EDS detected Fe, C, and O as the principal elements in the analyzed fields. XRD identified Fe, $FeCO_3$, Fe_2O_3, Fe_3O_4, and FeOOH (Figure 8). At 40 °C, the pattern was dominated by Fe substrate reflections, and no distinct $FeCO_3$ peak was resolved. $FeCO_3$ reflections appeared at 60 °C and became more prominent at 75 °C, while Fe substrate peaks remained visible. The combined SEM and XRD results therefore demonstrate a temperature-dependent increase in $FeCO_3$-containing surface products, together with persistent spatial heterogeneity and local spallation.

Temperature simultaneously influences electrochemical kinetics, mass transport, gas solubility, and $FeCO_3$ precipitation [15,16,35]. At 40 °C, the relatively slow reaction and transport rates resulted in limited corrosion-product coverage and comparatively low uniform and maximum pitting corrosion rates. Increasing the temperature to 60 °C accelerated both anodic dissolution and cathodic reactions, markedly increasing metal loss. Although $FeCO_3$ reflections appeared, the coarse aggregates and visible surface gaps provided only partial coverage, and both corrosion modes intensified. At 75 °C, the larger $FeCO_3$ contribution and greater coverage in some regions enhanced the barrier effect against average metal loss, causing the uniform corrosion rate to decrease slightly from its maximum at 60 °C. Rizzo et al. similarly showed that temperature strongly affects both corrosion kinetics and the nature and morphology of CO_2 corrosion products [35]. Nevertheless, the maximum pitting corrosion rate continued to increase because higher temperature accelerates ion transport and electrochemical dissolution within active pits. Cl^- enrichment and acidification caused by Fe^{2+} hydrolysis sustain the local autocatalytic process, allowing rapid pit propagation even where average surface coverage improves.

4. Conclusions

The individual effects of CO_2 partial pressure, O_2 partial pressure, Cl^- concentration, and temperature on N80 steel were evaluated under simulated coalbed–methane conditions. The principal conclusions are as follows:

(1) Increasing the CO_2 partial pressure from 0.10 to 1.00 MPa increased the uniform corrosion rate from 0.712 to 0.930 mm/a but decreased the maximum pitting corrosion rate from 1.691 to 0.280 mm/a. The higher CO_2 partial pressure increased the intensity of the $FeCO_3$ reflections and increased corrosion-product coverage, thereby reducing surface heterogeneity and suppressing maximum local penetration despite the continued increase in average metal loss.

(2) O_2 exerted the strongest simultaneous accelerating effect on uniform and localized corrosion. At 0.40 MPa O_2, the uniform and maximum pitting corrosion rates reached 1.446 and 2.202 mm/a, respectively. These increases were accompanied by coarse

products, extensive cracking, and spallation, demonstrating the importance of oxygen-control measures during coalbed–methane production and workover operations.

(3) Increasing the Cl^- concentration from 3 to 187 g/L decreased the uniform corrosion rate from 1.078 to 0.839 mm/a but increased the maximum pitting corrosion rate from 0.474 to 1.807 mm/a. High salinity therefore shifted the principal risk from average wall loss to localized penetration. Fine-grained product coverage reduced metal loss over parts of the surface, whereas exposed or damaged regions sustained autocatalytic pit growth.

(4) The uniform corrosion rate reached a maximum of 1.516 mm/a at 60 °C and decreased slightly at 75 °C, whereas the maximum pitting corrosion rate increased continuously to 2.202 mm/a. These contrasting trends reflect competition between accelerated electrochemical reactions and increasing $FeCO_3$-containing coverage, while elevated temperature continued to promote transport and dissolution within active pits.

(5) The corrosion products comprised $FeCO_3$, Fe_2O_3, Fe_3O_4, and FeOOH superimposed on diffraction from the Fe substrate. $FeCO_3$ was the principal crystalline corrosion product under the higher-CO_2 and higher-temperature conditions. Its protective contribution depended on the extent and visible integrity of surface coverage: broader, intact coverage was associated with lower maximum pitting, whereas cracking, spallation, and substrate exposure were associated with more severe localized corrosion.

For the target coalbed–methane block, corrosion management should prioritize prevention of oxygen ingress, targeted pitting protection in high-salinity sections, and differentiated surveillance of intermediate- and high-temperature intervals. Monitoring of gas composition, water chemistry, and temperature should be combined with appropriate corrosion inhibitors or material-protection measures and periodic inspection for both general wall thinning and localized damage. Future work will address longer exposure periods and dynamic-flow conditions and will use time-resolved electrochemical measurements to further quantify corrosion-product evolution and pit propagation.

Author Contributions: Conceptualization, J.L. and S.C.; methodology, J.L.; software, C.W.; validation, J.L., S.C. and X.C.; formal analysis, J.L. and B.Z.; investigation, J.L. and N.L.; resources, J.Z.; data curation, M.L. and B.Z.; writing—original draft preparation, J.L.; writing—review and editing, J.L., S.C. and X.C.; visualization, M.L.; supervision, C.W.; project administration, J.Z.; funding acquisition, J.Z. All authors have read and agreed to the published version of the manuscript.

Funding: This research was funded by the National Major Science and Technology Project of New Oil and Gas Exploration and Development "Enhanced Oil Recovery Technologies and Integrated Demonstration for Tight Sandstone Oil Reservoirs" (Project No. 2025ZD1405406).

Institutional Review Board Statement: Not applicable.

Informed Consent Statement: Not applicable.

Data Availability Statement: The original contributions presented in this study are included in this article.

Acknowledgments: The authors thank the State Key Laboratory of Oil and Gas Equipment for providing experimental support.

Conflicts of Interest: Authors Baojun Zheng, Chaoming Wang, and Juantao Zhang were employed by the State Key Laboratory of Oil and Gas Equipment, and author Ning Liu was employed by the Oil & Gas Technology Research Institute, PetroChina Changqing Oilfield Branch. The remaining authors declare that the research was conducted in the absence of any commercial or financial relationships that could be construed as potential conflicts of interest.

References

1. Mi, W.; Wen, H.; Fan, S.; Wei, G.; Liu, M.; Wang, S.; He, H.; Wu, X.; Cheng, X.; Liu, B.; et al. Pilot test of high-pressure water jet slotting with liquid CO_2 injection to displace CH_4 and improve coal seam permeability. *Fuel* **2023**, *351*, 128822. [CrossRef]
2. Hausler, R.H.; Stegmann, D.W. CO_2 corrosion and its prevention by chemical inhibition in oil and gas production. In *Proceedings of CORROSION 1988, St. Louis, MO, USA, 21–25 March 1988*; NACE International: Houston, TX, USA, 1988; p. 88363.
3. Lin, Y.; Wang, S.; Qiao, J.; Zhang, H.; Zhang, E.; Ma, Y.; Hao, Y. Chemical characteristics, formation mechanisms, and geological evolution processes of high-salinity coal reservoir water in the Binchang area of the southern Ordos Basin, China. *Int. J. Coal Geol.* **2024**, *291*, 104574. [CrossRef]
4. Zhang, F.; Jing, C.; Li, J.; Wang, B.; Ma, M.; Yi, T.; Hu, H. Low-frequency corrosion fatigue test study of sucker rods under high-salinity well fluids in deep CBM wells. *Processes* **2024**, *12*, 60. [CrossRef]
5. Hou, D.; Wu, X.; Zhang, Z.; Zhu, D.; Li, Y.; Lu, Q. Study on the corrosion and damage behaviours of P110 tubing of deep shale gas wells. *Corros. Eng. Sci. Technol.* **2025**, *60*, 47–61. [CrossRef]
6. Xiang, Y.; Wang, Z.; Xu, C.; Zhou, C.; Li, Z.; Ni, W. Impact of SO_2 concentration on the corrosion rate of X70 steel and iron in water-saturated supercritical CO_2 mixed with SO_2. *J. Supercrit. Fluids* **2011**, *58*, 286–294. [CrossRef]
7. Zhang, Y.; Gao, K.; Schmitt, G. Water effect on steel corrosion under supercritical CO_2 conditions. In *Proceedings of CORROSION 2011, Houston, TX, USA, 13–17 March 2011*; NACE International: Houston, TX, USA, 2011; p. 11378.
8. Teeter, L.; Repukaiti, R.; Huerta, N.; Oleksak, R.P.; Thomas, R.B.; Doğan, Ö.N.; Ziomek-Moroz, M.; Tucker, J.D. Effect of O_2 on the long-term operation and corrosion of steel X65 in CO_2–H_2O environments for direct supercritical CO_2 power cycle applications. *J. Supercrit. Fluids* **2019**, *152*, 104520. [CrossRef]
9. El Mendili, Y.; Abdelouas, A.; Bardeau, J.F. Insight into the mechanism of carbon steel corrosion under aerobic and anaerobic conditions. *Phys. Chem. Chem. Phys.* **2013**, *15*, 9197–9204. [CrossRef] [PubMed]
10. He, L.; Zhang, Q.; Chen, W.; Wang, Y.; Wang, M.; Huang, Y.; Xu, Y. Unraveling short-term O_2 contamination on under deposit corrosion of X65 pipeline steel in CO_2 saturated solution. *Corros. Sci.* **2024**, *233*, 112113. [CrossRef]
11. Wang, X.; Wang, X.; Wang, J.; Wang, G.; Pan, Y.; Yan, S. The influence of O_2 on the corrosion behavior of the X80 steel in CO_2 environment. *Int. J. Electrochem. Sci.* **2020**, *15*, 889–898. [CrossRef]
12. Song, F.M. A comprehensive model for predicting CO_2 corrosion rate in oil and gas production and transportation systems. *Electrochim. Acta* **2010**, *55*, 689–700. [CrossRef]
13. Leng, J.; Cheng, Y.F.; Liao, K.; Huang, Y.; Zhou, F.; Zhao, S.; Liu, X.; Zou, Q. Synergistic effect of O_2–Cl^- on localized corrosion failure of L245N pipeline in CO_2–O_2–Cl^- environment. *Eng. Fail. Anal.* **2022**, *138*, 106332. [CrossRef]
14. Sun, H.; Wu, X.; Han, E.H.; Wei, Y. Effects of pH and dissolved oxygen on electrochemical behavior and oxide films of 304SS in borated and lithiated high temperature water. *Corros. Sci.* **2012**, *59*, 334–342. [CrossRef]
15. Sun, W.; Nešić, S.; Woollam, R.C. The effect of temperature and ionic strength on iron carbonate ($FeCO_3$) solubility limit. *Corros. Sci.* **2009**, *51*, 1273–1276. [CrossRef]
16. Nešić, S. Key issues related to modelling of internal corrosion of oil and gas pipelines—A review. *Corros. Sci.* **2007**, *49*, 4308–4338. [CrossRef]
17. Dong, B.; Zeng, D.; Favero, C.; Divers, T.; Boisse, N.; Xu, Q.; Ling, J.; Xie, K.; Wang, Q. Insight into polymer concentration, temperature, CO_2 content, and Cl^- content on corrosion of N80 steel tubing in polymer flooding. *Mater. Corros.* **2023**, *74*, 943–961. [CrossRef]
18. Cheng, S.; Zhao, X.; Fu, A.; Li, D.; Yin, C.; Feng, Y. Corrosion behavior of J55 and N80 carbon steels in simulated formation water under different CO_2 partial pressures. *Coatings* **2022**, *12*, 1402. [CrossRef]
19. Kahyarian, A.; Brown, B.; Nešić, S. Electrochemistry of CO_2 corrosion of mild steel: Effect of CO_2 on the iron dissolution reaction. *Corros. Sci.* **2017**, *129*, 146–151. [CrossRef]
20. Nešić, S.; Lee, K.L.J. A mechanistic model for carbon dioxide corrosion of mild steel in the presence of protective iron carbonate films—Part 3: Film growth model. *Corrosion* **2003**, *59*, 616–628. [CrossRef]
21. Pessu, F.O.; Saleem, E.; Espejo, C.; Neville, A. Understanding the local pitting corrosion characteristics of carbon steel in CO_2 corrosion environment using artificially machined pits. *Results Eng.* **2022**, *16*, 100700. [CrossRef]
22. Shi, B.; Wang, X.; Zhou, K.; Xue, K.; Liu, K.; Zhang, X.; Qiu, Y. Study on the corrosion mechanism of N80 steel in simulated oxygen-reduced air drive production wellbores. *ACS Omega* **2023**, *8*, 24016–24022. [CrossRef] [PubMed]
23. Xue, F.; Wei, X.; Dong, J.; Etim, I.I.N.; Wang, C.; Ke, W. Effect of residual dissolved oxygen on the corrosion behavior of low carbon steel in 0.1 M $NaHCO_3$ solution. *J. Mater. Sci. Technol.* **2018**, *34*, 1349–1358. [CrossRef]
24. Basilico, E.; Marcelin, S.; Mingant, R.; Kittel, J.; Fregonese, M.; Barker, R.; Owen, J.; Neville, A.; Ropital, F. Effect of O_2 contamination on carbon steel pseudo-passive scales in CO_2 aqueous solutions. *Corros. Sci.* **2022**, *205*, 110388. [CrossRef]
25. Xia, L.; Li, Y.; Ma, L.; Zhang, H.; Li, N.; Jiang, Z. Influence of O_2 on the erosion-corrosion performance of 3Cr steels in CO_2 containing environment. *Materials* **2020**, *13*, 791. [CrossRef]

26. Ingham, B.; Ko, M.; Shaw, P.; Sk, M.H.; Abdullah, A.M.; Laycock, N.; Williams, D.E. Effects of oxygen on scale formation in CO_2 corrosion of steel in hot brine: In situ synchrotron X-ray diffraction study of anodic products. *J. Electrochem. Soc.* **2018**, *165*, C756–C761. [CrossRef]
27. da Silva, P.N.; Svenningsen, G.; Dugstad, A.; Gomes, J.A.C.P. The influence of oxygen on protective iron carbonate scales formed on carbon steel in CO_2 environments at near-neutral pH. In *Proceedings of the AMPP Annual Conference + Expo 2022, San Antonio, TX, USA, 6–10 March 2022*; AMPP: Houston, TX, USA, 2022; p. 17899.
28. Han, J.; Carey, J.W.; Zhang, J. Effect of sodium chloride on corrosion of mild steel in CO_2-saturated brines. *J. Appl. Electrochem.* **2011**, *41*, 741–749. [CrossRef]
29. Schmitt, G. Fundamental aspects of CO_2 metal loss corrosion. Part II: Influence of different parameters on the CO_2 corrosion mechanism. In *Proceedings of CORROSION 2015, Dallas, TX, USA, 15–19 March 2015*; NACE International: Houston, TX, USA, 2015; p. 6033.
30. Yue, X.; Zhang, L.; Liu, H.; Zhao, H.; Wang, S.; Hua, Y. Uncoupling chloride and acidification attack on the naturally formed corrosion scales. *Corros. Sci.* **2022**, *199*, 110207. [CrossRef]
31. Zhang, S.; Li, Y.; Wei, Y.; Liu, B.; Du, H.; Wei, H.; Hou, L. Synergistic effect of chloride ions and filmed surface on pitting in the pseudo-passivation behavior of carbon steel. *Vacuum* **2021**, *185*, 110042. [CrossRef]
32. Zhang, S.; Hou, L.; Du, H.; Wei, H.; Liu, B.; Wei, Y. A study on the interaction between chloride ions and CO_2 towards carbon steel corrosion. *Corros. Sci.* **2020**, *167*, 108531. [CrossRef]
33. Ma, Z.; Gao, X.; Brown, B.; Nešić, S.; Singer, M. Improvement to water speciation and $FeCO_3$ precipitation kinetics in CO_2 environments: Updates in NaCl concentrated solutions. *Ind. Eng. Chem. Res.* **2021**, *60*, 17026–17035. [CrossRef]
34. Mou, L.; Zhang, S.; Li, J.; Liu, B.; Yu, S.; Zhang, Y.; Xia, Y. Comprehending of the reverse effect of Cl^- concentration and fluid flow on pitting corrosion of carbon steel. *Vacuum* **2022**, *206*, 111547. [CrossRef]
35. Rizzo, R.; Baier, S.; Rogowska, M.; Ambat, R. An electrochemical and X-ray computed tomography investigation of the effect of temperature on CO_2 corrosion of 1Cr carbon steel. *Corros. Sci.* **2020**, *166*, 108471. [CrossRef]

Disclaimer/Publisher's Note: The statements, opinions and data contained in all publications are solely those of the individual author(s) and contributor(s) and not of MDPI and/or the editor(s). MDPI and/or the editor(s) disclaim responsibility for any injury to people or property resulting from any ideas, methods, instructions or products referred to in the content.